

Resonant scattering in galaxy clusters for anisotropic gas motions on various spatial scales

I.Zhuravleva^{1*}, E.Churazov^{1,2}, S.Sazonov^{2,1}, R.Sunyaev^{1,2}, K.Dolag¹

¹*Max Planck Institute for Astrophysics, Karl-Schwarzschild str. 1, Garching, 85741, Germany*

²*Space Research Institute, Profsoyuznaya str. 84/32, Moscow, 117997, Russia*

ABSTRACT

The determination of characteristic amplitudes and anisotropy of hot gas motions in galaxy clusters from observations of the brightest resonance lines is discussed. Gas motions affect (i) the spectral line shape through the Doppler effect and (ii) the radial surface brightness profiles in lines during resonant scattering. Radiative transfer calculations have been performed by the Monte Carlo method in the FeXXV resonance line at 6.7 keV for the Perseus cluster (Abell426). It was shown that (a) radial motions reduce the scattering efficiency much more dramatically than purely tangential motions; (b) large-scale gas motions weakly affect the scattering efficiency. The uncertainty in measuring the characteristics of gas motions using resonant scattering has been estimated for existing and future observations of clusters.

Key words: galaxy clusters, radiative transfer, scattering

1 INTRODUCTION

The intergalactic gas in galaxy clusters is the dominant (in mass) baryonic component and accounts for about 15% of the virial cluster mass. Falling into the potential well of a cluster, the gas heats up to a temperature of 2–10 keV. The presence of gas motions with velocities of hundreds and thousands km s^{-1} in galaxy clusters is indirectly confirmed both by high-angular-resolution X-ray data, namely the observations of substructure in surface brightness and temperature distributions (e.g. see the review by Markevitch and Vikhlinin (2007)), and by numerical simulations, which show gas motions on various spatial scales, both far from the center and in the central regions of clusters (Norman and Bryan (1999); Inogamov and Sunyaev (2003); Dolag et al. (2005); Vazza et al. (2009)).

The anisotropy, velocity amplitudes and scales of the motions along the line-of-sight can be determined from the shift and broadening of spectral lines (e.g. see Inogamov and Sunyaev (2003)). However, measurements with a sufficient energy resolution will become possible only after the launch of an X-ray microcalorimeter on-board of the ASTRO-H mission with an energy resolution of ~ 4 eV at 6 keV (Mitsuda 2009). For example, for the FeXXV line at 6.7 keV, a shift of ~ 10 eV emerges during gas motions with a velocity

of 500 km s^{-1} . The tangential component of gas motions is even more difficult to determine¹. Another method for diagnostics of gas motions is based on analysis of the scattering in bright lines in the spectra of galaxy clusters (e.g. see the review by Churazov et al. (2010)). The characteristic amplitudes of gas motions in galaxy clusters (Churazov et al. 2004; Sanders et al. 2010) and elliptical galaxies (e.g. see Xu et al. (2002); Werner et al. (2009)) have been estimated by comparing the surface brightness profiles in optically thin and thick lines of the same ion. Finally, information about the power spectrum of the velocities of gas motions can be obtained by considering the surface brightness or pressure fluctuations. For example, using a Fourier analysis of the surface brightness and gas temperature fluctuations in the Coma cluster (A1656), Schuecker et al. (2004) claimed the power spectrum of gas motions to be a Kolmogorov one. A Kolmogorov turbulence power spectrum was also obtained by Vogt and Enßlin (2003) using measurements of the spatial Faraday rotation fluctuations.

In this paper, we are interested in what information about the gas motions we can obtain by considering the distortions of the surface brightness profiles in resonance lines. We are interested in the reliability of determining the

¹ Zhuravleva et al. (2010) proposed a method for determination of tangential gas velocities based on analysis of the polarization in resonance X-ray lines.

* izhur@mpa-garching.mpg.de

directions, amplitudes and spatial scales of gas motions in real clusters from resonant scattering observations.

The velocity of ion motions can be represented as $\mathbf{V} = \mathbf{V}_{\text{bulk}} + \mathbf{V}_{\text{turb}} + \mathbf{V}_{\text{therm}}$. Here, \mathbf{V}_{bulk} are the large-scale (bulk) gas motions that affect both the line broadening and the energy shift at the line center; \mathbf{V}_{turb} are the gas motions on scales smaller than any characteristic sizes, in particular, the size of the region inside which the optical depth in lines > 1 (microturbulent motions), that cause only line broadening; and $\mathbf{V}_{\text{therm}}$ are the thermal ion motions leading to the line broadening. Under conditions of galaxy clusters, the thermal broadening of heavy-element lines can be much smaller than that for other types of motions.

In this paper, we separately consider the influence of large- and small-scale gas motions on the line profiles and resonant scattering. The cluster model used and details of our calculations are described. The main results and conclusions are discussed.

2 LINE PROFILES

2.1 The Influence of Microturbulent Gas Motions on the Line Profiles

As has been mentioned above, we will use the term “microturbulence” to describe motions with spatial scales of velocity variations much smaller than any characteristic size present in the problem. Such motions lead to line broadening.

Microturbulence can arise, for example, from the mergers of clusters, from buoyant bubbles of relativistic plasma or convection caused by the mixing of thermal plasma and cosmic rays. Talking about turbulence, one usually refers to gas motions with the same velocity dispersion in all directions. However, the cases when anisotropic turbulence, radial and tangential, appears are possible. For example, purely radial motions naturally arise if the energy from the central active galactic nucleus (AGN) powers shocks and sound waves that propagate through the intergalactic medium mainly in the radial direction away from the central source (e.g. see Forman et al. (2005, 2007); Fabian et al. (2003, 2006)). In contrast, tangential motions can naturally emerge in stratified atmospheres, where internal waves carry the energy of vertical motions away from the region of space under consideration. This can give rise to two dimensional (tangential) motions (Churazov et al. 2001, 2002; Rebusco et al. 2008).

Let consider how the anisotropy of turbulent gas motions changes the spectral line profiles. Let us assume that the gas as a whole is at rest at each point of the cluster and there is a Gaussian ion velocity distribution,

$$P(V_r, V_\theta, V_\phi) = \frac{1}{(2\pi)^{3/2} \sigma_r \sigma_\theta \sigma_\phi} \times \exp \left[-\frac{1}{2} \left(\frac{V_r}{\sigma_r} \right)^2 - \frac{1}{2} \left(\frac{V_\theta}{\sigma_\theta} \right)^2 - \frac{1}{2} \left(\frac{V_\phi}{\sigma_\phi} \right)^2 \right], \quad (1)$$

where r, θ, ϕ are three spatial coordinates at a given point (in the radial and tangential directions) and the set of three quantities $\Sigma^2 = (\sigma_r^2, \sigma_\theta^2, \sigma_\phi^2)$ characterizes the velocity dispersion in these directions. Writing the ion velocity vector

in some direction $\mathbf{m} = (m_r, m_\theta, m_\phi)$ as $\mathbf{V} = V\mathbf{m}$, the probability that the projection of the ion velocity vector onto the direction \mathbf{m} at a given point of space will be V is

$$P(V) = \frac{1}{\sqrt{2\pi}\sigma_{\text{eff}}} \exp \left[-\frac{1}{2} \left(\frac{V}{\sigma_{\text{eff}}} \right)^2 \right], \quad (2)$$

where σ_{eff} can be represented as (given only the broadening due to turbulence)

$$\sigma_{\text{eff}}^2 = (\sigma_{\text{turb},r} m_r)^2 + (\sigma_{\text{turb},\theta} m_\theta)^2 + (\sigma_{\text{turb},\phi} m_\phi)^2. \quad (3)$$

Clearly, for isotropic turbulence, the velocity dispersion in all directions is the same, i.e. $\sigma_{\text{turb},r} = \sigma_{\text{turb},\theta} = \sigma_{\text{turb},\phi}$. For radial turbulence, only the radial component remains and, accordingly, for tangential turbulence, the radial component of the velocity dispersion is zero. Thus, these three cases can be described as follows:

$$\Sigma^2 = \begin{cases} (\sigma_{\text{turb},r}^2, \sigma_{\text{turb},\theta}^2, \sigma_{\text{turb},\phi}^2), \text{ isotropic} \\ (\sigma_{\text{turb},r}^2, 0, 0), \text{ radial} \\ (0, \sigma_{\text{turb},\theta}^2, \sigma_{\text{turb},\phi}^2), \text{ tangential} \end{cases} \quad (4)$$

The kinetic energy is related to the velocity dispersion as $\varepsilon_{\text{kin}} = \frac{1}{2} \rho (\sigma_{\text{turb},r}^2 + \sigma_{\text{turb},\theta}^2 + \sigma_{\text{turb},\phi}^2)$. Fixing the kinetic energy in all velocity components, we obtain

$$\Sigma^2 = \begin{cases} (\frac{2}{3\rho} \varepsilon_{\text{kin}}, \frac{2}{3\rho} \varepsilon_{\text{kin}}, \frac{2}{3\rho} \varepsilon_{\text{kin}}), \text{ isotropic} \\ (\frac{2}{\rho} \varepsilon_{\text{kin}}, 0, 0), \text{ radial} \\ (0, \frac{1}{\rho} \varepsilon_{\text{kin}}, \frac{1}{\rho} \varepsilon_{\text{kin}}), \text{ tangential} \end{cases} \quad (5)$$

Substituting (5) into (3), we find σ_{eff}^2 at fixed total kinetic energy of turbulent motions:

$$\sigma_{\text{eff}}^2 = \begin{cases} \frac{2}{3\rho} \varepsilon_{\text{kin}}, \text{ isotropic} \\ \frac{2}{\rho} \varepsilon_{\text{kin}} \cos^2(\alpha), \text{ radial} \\ \frac{1}{\rho} \varepsilon_{\text{kin}} \sin^2(\alpha), \text{ tangential} \end{cases}, \quad (6)$$

where α is the angle between the direction of photon motion \mathbf{m} and the radius vector.

Analogously we can derive expressions for σ_{eff} by fixing not the total energy but the velocity dispersion ξ in a given direction. Assuming that $\sigma_{\text{turb},r} = \sigma_{\text{turb},\theta} = \sigma_{\text{turb},\phi} = \xi$ for isotropic turbulence, $\sigma_{\text{turb},r} = \xi$, $\sigma_{\text{turb},\theta} = \sigma_{\text{turb},\phi} = 0$ for radial turbulence, and $\sigma_{\text{turb},r} = 0$, $\sigma_{\text{turb},\theta} = \sigma_{\text{turb},\phi} = \xi$ for tangential turbulence, we obtain

$$\sigma_{\text{eff}}^2 = \begin{cases} \xi^2, \text{ isotropic} \\ \xi^2 \cos^2(\alpha), \text{ radial} \\ \xi^2 \sin^2(\alpha), \text{ tangential} \end{cases} \quad (7)$$

To calculate the spectral line profile from the entire cluster, let consider a spherically symmetric cluster and an infinitely thin, homogeneous spherical shell at distance $r = 1$ from the cluster center. The shell thickness along the line-of-sight is approximately equal to $\frac{\Delta r r}{\sqrt{r^2 - R^2}} = \frac{\Delta r}{\sqrt{1 - R^2}}$,

where Δr is the shell thickness in the radial direction and R is the projected radius in the plane of the sky. Let V be the velocity along the line-of-sight and the Gaussian ion velocity distribution (2) be valid. We will take into account only the turbulent line broadening, i.e., $\sigma_{\text{eff}}^2 = (\sigma_{\text{turb},r} m_r)^2 + (\sigma_{\text{turb},\theta} m_\theta)^2 + (\sigma_{\text{turb},\phi} m_\phi)^2$. At fixed velocity dispersion in a given direction Eq. (7) will then be rewritten as

$$\sigma_{\text{eff}}^2 = \begin{cases} \xi^2, \text{isotropic} \\ \xi^2(1 - R^2), \text{radial} \\ \xi^2 R^2, \text{tangential} \end{cases} \quad (8)$$

Substituting (8) into (2) and integrating (2) over the area RdR , we obtain the following line profiles for isotropic, radial and tangential turbulence:

$$\begin{aligned} & \int_0^1 \frac{\Delta r}{\sqrt{2\pi}s} \frac{R}{\sqrt{1-R^2}} \\ & \times \exp\left(-\frac{1}{2} \frac{V^2}{s^2}\right) dR, \text{isotropic} \\ & \int_0^1 \frac{\Delta r}{\sqrt{2\pi}\sqrt{1-R^2}s} \frac{R}{\sqrt{1-R^2}} \\ & \times \exp\left(-\frac{1}{2} \frac{V^2}{s^2(1-R^2)}\right) dR, \text{radial} \\ & \int_0^1 \frac{\Delta r}{\sqrt{2\pi}Rs} \frac{R}{\sqrt{1-R^2}} \\ & \times \exp\left(-\frac{1}{2} \frac{V^2}{s^2 R^2}\right) dR, \text{tangential} \end{aligned} \quad (9)$$

where $s = \xi$. The expressions for the line profiles at fixed total kinetic energy are similar but with the substitution $s = 2\varepsilon_{\text{kin}}/3\rho, 2\varepsilon_{\text{kin}}/\rho, \varepsilon_{\text{kin}}/\rho$ for isotropic, radial and tangential turbulence, respectively. Figure 1 shows the derived averaged profiles that agree well with those from our numerical simulations in the limit of a low temperature and a large amplitude of gas motions. Note that the root-mean-square (rms) line widths at fixed kinetic energy of turbulent motions are identical for any anisotropy, although the line shapes do not coincide.

The change in line width with distance from the cluster center for various types of turbulence was considered by Rebusco et al. (2008). It was shown that the linewidth is constant along the radius for isotropic turbulence, the lines are considerably broader at the cluster center than at the edges for radial turbulence, and, on the contrary, the broadest lines are at the cluster edges for tangential turbulence.

2.2 The Influence of Large-Scale Gas Motions on the Line Profiles

As was said in the Introduction, large-scale gas motions cause the lines to be shifted and broadened. This is easy

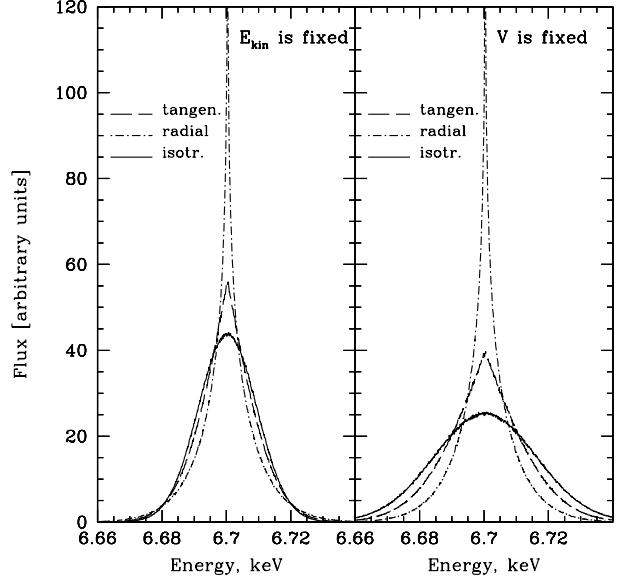


Figure 1. Analytical spectral profiles of the helium-like iron line at 6.7 keV for isotropic microturbulent (solid curves), radial (dash-dotted curves) and tangential (dashed curves) gas motions. The line broadening only due to turbulence is taken into account. The profiles were calculated at fixed total kinetic energy and fixed velocity amplitude of gas motions (9).

to see using the results of numerical simulations of galaxy clusters. Figure 2 shows the spectral profiles of the helium-like iron line at 6.7 calculated for the model cluster g676, which is an example of a low-mass, dynamically quiet cold cluster (see the “Velocity Field” Section and Table 1) by taking into account the large-scale motions and thermal line broadening. The profiles were calculated for nine lines-of-sight. For the central panel, the line-of-sight passes through the cluster center. The thin solid curves indicate the spectra that emerge in the case of purely thermal broadening; the profiles in the presence of gas motions are indicated by the thick solid curves. The dashed curves indicate the Gaussian line profile fits. The profiles averaged over the entire cluster are shown in Fig. 3. We see that the profiles are broadened and shifted in the presence of gas motions. Strong deviations from the Gaussian profile are clearly seen at the cluster periphery, suggesting the presence of large-scale gas motions.

Depending on which cluster region we observe (the cluster center or edge), the line profiles will be more sensitive to radial or tangential gas motions. This is demonstrated in Fig. 4, where the spectral profiles of the helium-like iron line at 6.7 keV are shown for the model, dynamically quiet cluster g6212 (see the “Velocity Field” Section and Table 1) calculated in three cluster regions: the central region (~ 70 kpc in diameter) and two regions at a projected distance of ~ 160 kpc from the center (~ 145 kpc in diameter each). We separately consider the influence of radial (dots) and tangential (dashes) gas motions and compare with the profiles in the case when the gas is at rest (solid curves). For this purpose, we set the radial, tangential, or both velocity components

Table 1. Basic parameters of the galaxy clusters from numerical simulations.

Cluster	$M_{\text{vir}, 10^{14} M_{\odot}}$	$R_{\text{vir}, \text{ Mpc}}$	$T_{\text{mean}, \text{ keV}}$
g6212	1.61	1.43	1.5
g8	32.70	3.90	13
g51	19.21	3.26	8.6
g676	1.60	1.43	1.25

equal to zero in each cell of the computational volume and repeated the radiative transfer computation procedure. We exclude the motion of the cluster as a whole by subtracting the weighted mean (within a sphere at the cluster center 50 kpc in radius) velocity.

In the cluster center the scale of gas motions is small compared to the size of the central region. Therefore, we see an almost symmetric and slightly broadened line. At the cluster edges, the spatial scale of gas motions is comparable to the characteristic size of the region that makes a dominant contribution to the emission. Therefore, we see an asymmetric line with a shift of the central energy. Since the surface brightness and (gas density) rapidly falls toward the cluster edges, the regions along the line-of-sight located near the plane of the sky passing through the cluster center make a major contribution to the emission. Obviously, the observed energy shift for these regions is produced mainly by tangential motions.

3 THE INFLUENCE OF THE VELOCITY FIELD ON RESONANT SCATTERING

The photon scattering probability in a given line is determined by (a) the optical depth at the line center, (b) the deviation of the photon energy from the line energy, and (c) the line width.

Turbulent gas motions in the direction of photon propagation will broaden the line, reducing the optical depth and the resonant scattering effect (see, e.g., Gilfanov et al. (1987)). Indeed, the optical depth at the line center can be found as $\tau = \int_0^{\infty} n_i s_0 dl$, where n_i is the ion number density and s_0 is the scattering cross section at the line center:

$$s_0 = \frac{\sqrt{\pi} h r_e c f}{\Delta E_D}, \quad (10)$$

Here, r_e is the classical electron radius, f is the oscillator strength of a given transition, and ΔE_D is the Doppler line width. The line broadening ΔE_D can be divided into two components: the purely thermal broadening and the broadening due to turbulent motions, i.e.,

$$\Delta E_D = \frac{E_0}{c} \sqrt{2(\sigma_{\text{therm}}^2 + \sigma_{\text{turb}}^2)}. \quad (11)$$

Here, σ_{turb} is the velocity dispersion due to turbulent motions and σ_{therm} is the thermal dispersion of ion velocities:

$$\sigma_{\text{therm}}^2 = \frac{kT}{Am_p}, \quad (12)$$

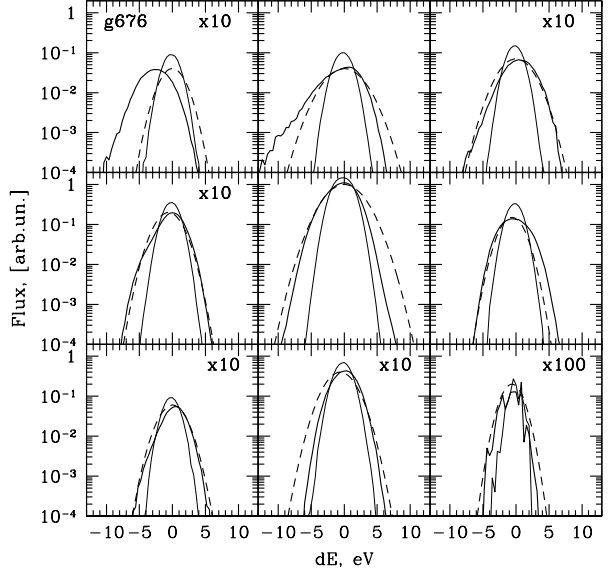


Figure 2. Profiles of the helium-like iron FeXXV line at 6.7 keV for nine lines-of-sight in the model cluster g676 (see the table). The cluster was divided into nine identical parts; the size of the entire cube is $1 \times 1 \times 1$ Mpc. For the central panel, the line of sight passes through the cluster center. The thick, thin and dashed curves indicate, respectively, the line profiles shifted and broadened through gas motions, the profiles emerging only in the case of thermal line broadening, and the Gaussian line profiles broadened through the mean temperature and V_{rms} in each region.

E_0 is the energy at the line center, k is the Boltzmann constant, m_p is the proton mass, A is the atomic weight of the element, and c is the speed of light. For heavy elements A is large (e.g., $A = 56$ for iron), therefore the thermal broadening of heavy-element lines is noticeably suppressed, while the broadening through gas motions is the same for all lines.

The presence of large-scale gas motions leads to a change in the resonant scattering cross section. In the reference frame of the gas, the cross section is proportional

$$\text{to } \exp \left\{ -\frac{\left(E \left[1 - \frac{(\mathbf{V}\mathbf{m})}{c} \right] - E_0 \right)^2}{2\sigma^2} \right\}, \text{ where } E \text{ is the photon}$$

energy in the reference frame of the cluster, E_0 is the transition energy, \mathbf{V} is the velocity of large-scale gas motions, \mathbf{m} is the photon propagation direction, and σ is the Gaussian line width determined by the thermal broadening and the broadening through turbulent gas motions.

4 CLUSTER MODEL AND SCATTERING CALCULATION

At present, the gas density and temperature distributions in nearby X-ray bright galaxy clusters, such as Perseus cluster, are well known. At the same time, there is almost no information about the properties of the gas velocity field. It seems natural to supplement the density and temperature

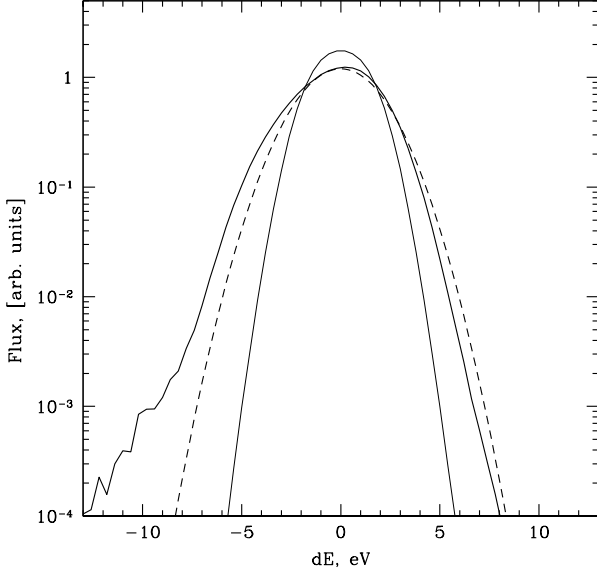


Figure 3. Profiles of the helium-like iron FeXXV line at 6.7 keV averaged over the entire model cluster g676. The notation is the same as that in Fig. 2.

measurements with the results of numerical hydrodynamic velocity calculations and to use such a combined model to model the resonant scattering.

4.1 Gas Temperature and Density Distributions

The resonant scattering calculations were performed for the Perseus galaxy cluster A426, whose electron temperature and density profiles were taken from Churazov et al. (2003). Correcting the profile for the Hubble constant $H_0 = 72 \text{ km s}^{-1} \text{ Mpc}^{-1}$, we find the electron density in cm^{-3} as

$$n_e = \frac{4.68 \cdot 10^{-2}}{\left(1 + \left(\frac{r}{56}\right)^2\right)^{3/2 \cdot 1.2}} + \frac{4.86 \cdot 10^{-3}}{\left(1 + \left(\frac{r}{194}\right)^2\right)^{3/2 \cdot 0.58}}. \quad (13)$$

The temperature distribution in keV is

$$T_e = 7 \frac{1 + \left(\frac{r}{100}\right)^3}{2.3 + \left(\frac{r}{100}\right)^3}, \quad (14)$$

where r is in kpc. The iron abundance is assumed to be constant in the cluster and equal to 0.5 of the solar one from the tables by Anders and Grevesse (1989) and 0.74 of the solar if one uses the newer tables by Asplund et al. (2009).

The mean temperature in the Perseus cluster is about 5-6 keV. At such temperatures, the strongest line in the spectrum is the K_α line of helium-like iron at 6.7 keV that corresponds to the $1s^2(^1S_0) - 1s2p(^1P_1)$ transition with an oscillator strength ~ 0.7 . The optical depth in this line from the cluster center to infinity is ~ 3 .

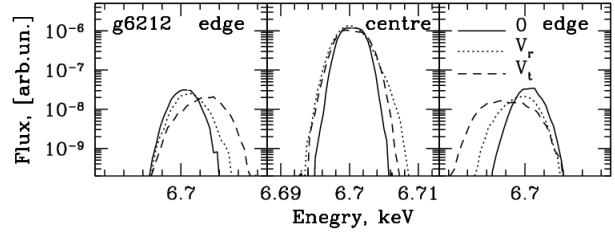


Figure 4. Spectral profile of the helium-like iron FeXXV line at 6.7 keV calculated for the model cluster g6212 (see the table) at the cluster center (the size is ~ 70 kpc) and in two regions at a distance of 160 kpc from the center (the size is ~ 145 kpc). The solid, dotted, and dashed curves indicate, respectively, the profiles when the gas is at rest, in the case of radial gas motions, and in the case of tangential gas motions.

4.2 Velocity Field

The energy resolution of modern X-ray telescopes does not allow the gas velocity field in galaxy clusters to be measured directly. To make the assumption about the velocity field, we will use the results of numerical cluster simulations taken from the cosmological calculations of the large-scale structure (Dolag et al. 2005; Springel et al. 2001). The numerical simulations give the three-dimensional structure of the gas density and temperature and three velocity components determined in a cube with a size of several Mpc. We considered nine clusters differing in mass. The rms velocity amplitudes in the coldest and hottest clusters are ~ 200 and $\sim 1000 \text{ km s}^{-1}$, respectively.

To make the conclusion about the directions of motions, let us compare the rms amplitude of the radial velocity V_r with that of the tangential one $\sqrt{(V_\theta^2 + V_\phi^2)/2}$. We exclude the motion of the cluster as a whole by subtracting the weighted mean (within a sphere at the cluster center 50 kpc in radius) velocity. The rms amplitude V_{rms} was calculated in spherical shells with radius r and thickness $\Delta r = 0.1r$ separately for the velocity components along and perpendicular to the radius. The results for the available nine clusters show that the gas motions are almost isotropic. Figure 5 presents the results for three clusters. The rms amplitudes of the velocities of radial gas motions are indicated by the dashed curves; the solid curves indicate the amplitudes for each velocity component in the tangential direction. We see that the curves differ insignificantly at radii $< 300 - 400$ kpc and, hence, the amplitudes of the gas motions are identical in all directions.

Although the assumption that the gas motions are isotropic is justified by our numerical simulations, it should be remembered that in reality the gas motions are not necessarily isotropic. For example, considering the velocities of gas filaments in H_α in the Perseus cluster, Hatch et al. (2006) showed that the gas at distances larger than 30 kpc from the central galaxy (i.e., where the resonant scattering is significant) entrained by AGN-inflated plasma bubbles is involved predominantly into radial motions.

To make reasonable assumptions about the properties

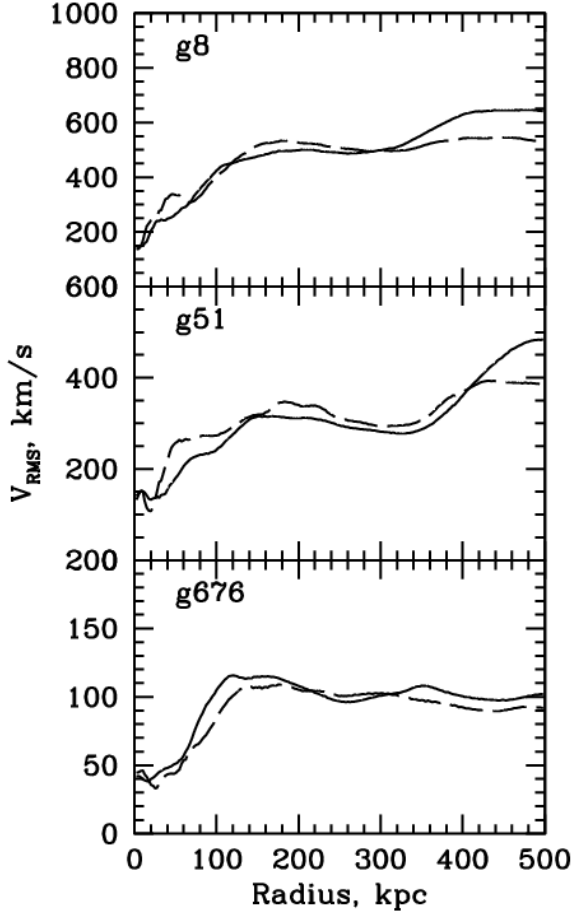


Figure 5. Rms amplitudes of the radial velocity of gas motions (dashed curves) and rms amplitudes of the tangential velocity $\sqrt{(V_\theta^2 + V_\phi^2)/2}$ (solid curves) versus distance from the cluster center for three model clusters taken from numerical simulations.

of the velocity field in our radiative transfer calculations, we analyzed the power spectra found in hydrodynamic simulations of cluster formation. An example for one cluster is shown in Fig. 6. Details of the method for calculating the power spectrum are given in Arevalo et al. (2011). Most of the numerical simulations suffer from an insufficient dynamic range of wave numbers needed to reliably determine the shape of the power spectrum. In particular, adaptive smoothing, which is especially significant for the SPH method (the solid curve in Fig. 6), leads to a cutoff in the power spectrum at large k . At the same time, non-adaptive smoothing leads to a sharp rise of the power spectrum at large wave numbers, which is related to Poissonian noise on these scales, in particular, when there are no particles at all within the cell. The true power spectrum at large k must lie between the dashed and solid curves shown in Fig. 6. The cutoff in the power spectrum at small wave numbers is related, in particular, to the choice of the size of the computa-

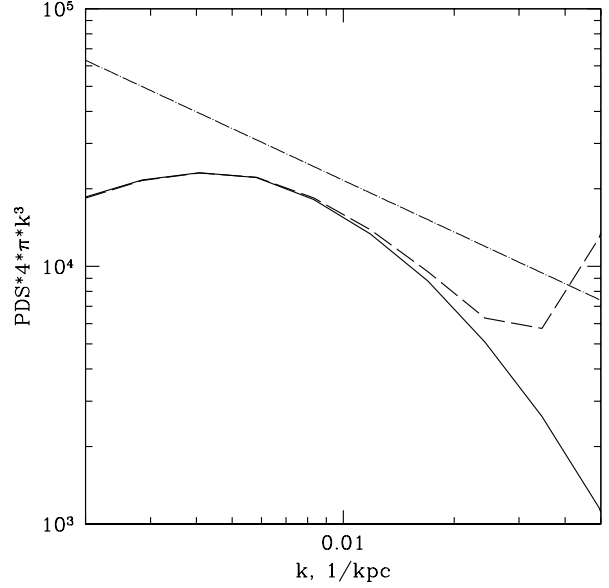


Figure 6. Power spectrum of the velocities of gas motions in the cluster g676 (see the table) from numerical simulations. To construct the spectra, we used the results of SPH simulations smoothed adaptively (solid curve) and non-adaptively (dashed curve). The Kolmogorov power spectrum $\sim k^{-2/3}$ is indicated by the dash-dotted curve.

tional volume centered on the cluster. We discuss this effect in a separate publication (Zhuravleva et al. 2011). In Fig. 6, the dash-dotted curve indicates the Kolmogorov power spectrum² $\sim k^{-2/3}$. One can see that the assumption about a Kolmogorov spectrum appears as a reasonable compromise, although the Kolmogorov slope in the simulated clusters is observed in a fairly narrow range of wave numbers.

Yet another problem can be associated with an insufficient resolution of SPH simulations on small scales. The scales that are resolved in simulations range from tens of kpc at the cluster center to several hundred kpc at the edges. An additional spatial scale arises in the scattering problem - the characteristic photon mean free path in scattering, i.e., the size at which an optical depth of the order of unity is accumulated. It is useful to compare this scale with the resolution of SPH simulations. For the cluster g676, the power spectrum is shown in Fig. 6; we see that on $k \leq 0.02 \text{ kpc}^{-1}$ the simulations are resolved. On shorter scales (large wave numbers), the calculations of the velocity field with an adaptive window (solid curve) and a non-adaptive window (dashed curve) give large difference in results. This discrepancy means that the simulation resolution limit was reached. The corresponding spatial scale³ is $\sim 50 \text{ kpc}$. In this case,

² The Kolmogorov spectrum has such a slope when the total energy associated with the motions with a given scale of wave numbers k is considered.

³ We use the relation $k = 1/l$ between the spatial scales and wave numbers without the factor 2π .

an optical depth of the order of unity near the cluster center is accumulated at a size $1/(n_i s_0) \sim 150$ kpc. Thus, the resolution of our simulations is sufficient for our purposes.

In the subsequent simulations, we assumed the power spectrum of the velocity fluctuations to be $k^3 P(k) \sim k^{-2/3}$.

4.3 Monte Carlo Simulations of Scattering

To simulate multiple scattering, we used the Monte Carlo method (Pozdnyakov et al. 1983). Details of the simulations of scattering in lines are discussed in Sazonov et al. (2002); Churazov et al. (2004) and Zhuravleva et al. (2010). The line energies and oscillator strengths were taken from the ATOMDB⁴ and NIST Atomic Spectra Database⁵ databases.

During the scattering, the photon direction \mathbf{m} is selected by taking into account the scattering phase function, which is a combination of Rayleigh and isotropic scattering phase functions (Hamilton 1947; Chandrasekhar 1950). For isotropic scattering, the new photon direction \mathbf{m}' is drawn randomly. For Rayleigh scattering, the probability that the photon after its scattering will propagate in the direction \mathbf{m}' is $P(\mathbf{m}', \mathbf{e}') \propto (\mathbf{e}' \cdot \mathbf{e}')^2$, where the direction of the electric field is $\mathbf{e}' = (\mathbf{e} - \mathbf{m}' \cos(\alpha)) / (\sqrt{1 - \cos^2(\alpha)})$ and α is the angle between the electric vector \mathbf{e} before the scattering and the new photon direction \mathbf{m}' , i.e. $\cos(\alpha) = (\mathbf{e} \cdot \mathbf{m}')$.

The initial photon position (or initial weight) is chosen in accordance with the volume emissivity of various cluster regions. To calculate the line emissivity, we used the APEC code (Smith et al. 2001). The ionization balance was taken from Mazzotta et al. (1998). For a randomly chosen initial direction of photon propagation \mathbf{m} , we find the photon energy E with a Gaussian distribution with mean E_0 and standard deviation $\Delta E_D / \sqrt{2}$, where ΔE_D was found from Eq. (11). Since the gas density is low, the pressure effects on the line broadening are neglected. We also neglect the contribution from the radiative decay of levels to the broadening by assuming the levels to be infinitely thin. When simulating the scattering process, we find the velocity of the scattering ion in such a way that the photon energy in the reference frame of the ion is exactly equal E_0 and the scattering occurs. Thus, the ion velocity in the direction of photon motion is $V_{\text{ion}} = (1 - \frac{E_0}{E})c$. We find the other two ion velocity components V_{ion1} and V_{ion2} in the directions \mathbf{m}_1 and \mathbf{m}_2 orthogonal to \mathbf{m} as $(\mathbf{V}_{\text{gas}}, \mathbf{m}_1) + V_{\text{gauss}}$ and $(\mathbf{V}_{\text{gas}}, \mathbf{m}_2) + V_{\text{gauss}}$, where V_{gauss} is the velocity with a Gaussian distribution. We take into account the velocity dispersion in the directions \mathbf{m}_1 and \mathbf{m}_2 according to Eqs. (7) or (6). As a result, the velocity of the scattering ion is $\mathbf{V}_{\text{tot}} = V_{\text{ion}}\mathbf{m} + V_{\text{ion1}}\mathbf{m}_1 + V_{\text{ion2}}\mathbf{m}_2$. Accordingly, after the selection of a new photon direction by taking into account the scattering phase matrix, we find the photon energy after the scattering as $E = E_0 (1 + (\mathbf{V}_{\text{tot}} \cdot \mathbf{m}')/c)$. In this case, we neglect the change in photon direction when going from the laboratory reference frame to the reference frame of the ion and vice versa, because $V/c \ll 1$. This approximation also assumes the velocity field and the gas distribution to

be constant on the time scales of the photon propagation through the cluster.

5 RESULTS

To calculate the influence of the velocity field on the scattering, we generate a random realization of the power spectrum with a given shape and normalization for each velocity component and make the inverse Fourier transform to obtain the velocity field with given properties.

We performed our calculations for three velocity fields.

A. The regime of microturbulence: there are no large-scale motions, microturbulence leads to line broadening through isotropic, radial, and tangential turbulence with $V_{\text{rms}} = 500 \text{ km s}^{-1}$.

B. The sensitivity to large-scale gas motions: the power spectrum is flat at small k up to k_s and then falls off as the Kolmogorov one (see Fig. 8c). In this case, the flat power spectrum at small k implies the absence of large-scale motions with sizes $> 1/k_s$. The bulk of the power is related to wave numbers of the order of k_s . Our calculations were performed for several values of k_s (l_s): 0.005 kpc^{-1} (200 kpc), 0.05 kpc^{-1} (20 kpc), and 0.2 kpc^{-1} (5 kpc). The rms amplitude of the velocity V_{rms} is 500 km s^{-1} in all cases.

C. The sensitivity to small-scale motions: the power spectrum is cut off at $k > k_s$ (see Fig. 8d); in this case, the decrease in the characteristic amplitude of the velocity is compensated by the line broadening, i.e., the power is transferred to microturbulence (the shortest scales).

In all three cases, the total energy in large- and small-scale motions is the same. The results are presented in Figs. 7 and 8 (corresponding to cases A, B, and C).

Figure 7 shows the ratio of the fluxes in the helium-like iron line at 6.7 keV with and without scattering in the case when there are no gas motions and in the case of different microturbulence designated in the figure (case A). The case of fixed velocity amplitude is indicated by the thick curves. The corresponding results of our calculations at fixed total energy are indicated by the thin curves. We see that when the gas is at rest, the optical depth is maximal, the line flux at the cluster center is strongly suppressed and the flux at the edges increases due to the scattering. When the gas motions are tangential, it is clear that the optical depth in the line calculated in the radial direction will not change. Since the photons produced in the cluster center moving in the radial direction make a major contribution to the scattering, the changes in brightness profiles are insignificant. The radial gas motions that directly affect the optical depth for the photons emerging from the cluster center and that reduce considerably the scattering efficiency have the strongest effect on the resonant scattering. Note that the optical depth in this case decreases by almost a factor of 3. Clearly, the case of isotropic turbulence is intermediate.

Considering large-scale gas motions (case B), note that when the bulk of the power of the motions is on large scales, the scattering is almost as efficient as that in the case when the gas is at rest (Fig. 8a, the curve with long dashes). In this case, a bulk motion of large gas volumes (the scales

⁴ <http://cxc.harvard.edu/atomdb/WebGUIDE/index.html>.

⁵ <http://physics.nist.gov/PhysRefData/ASD/index.html>.

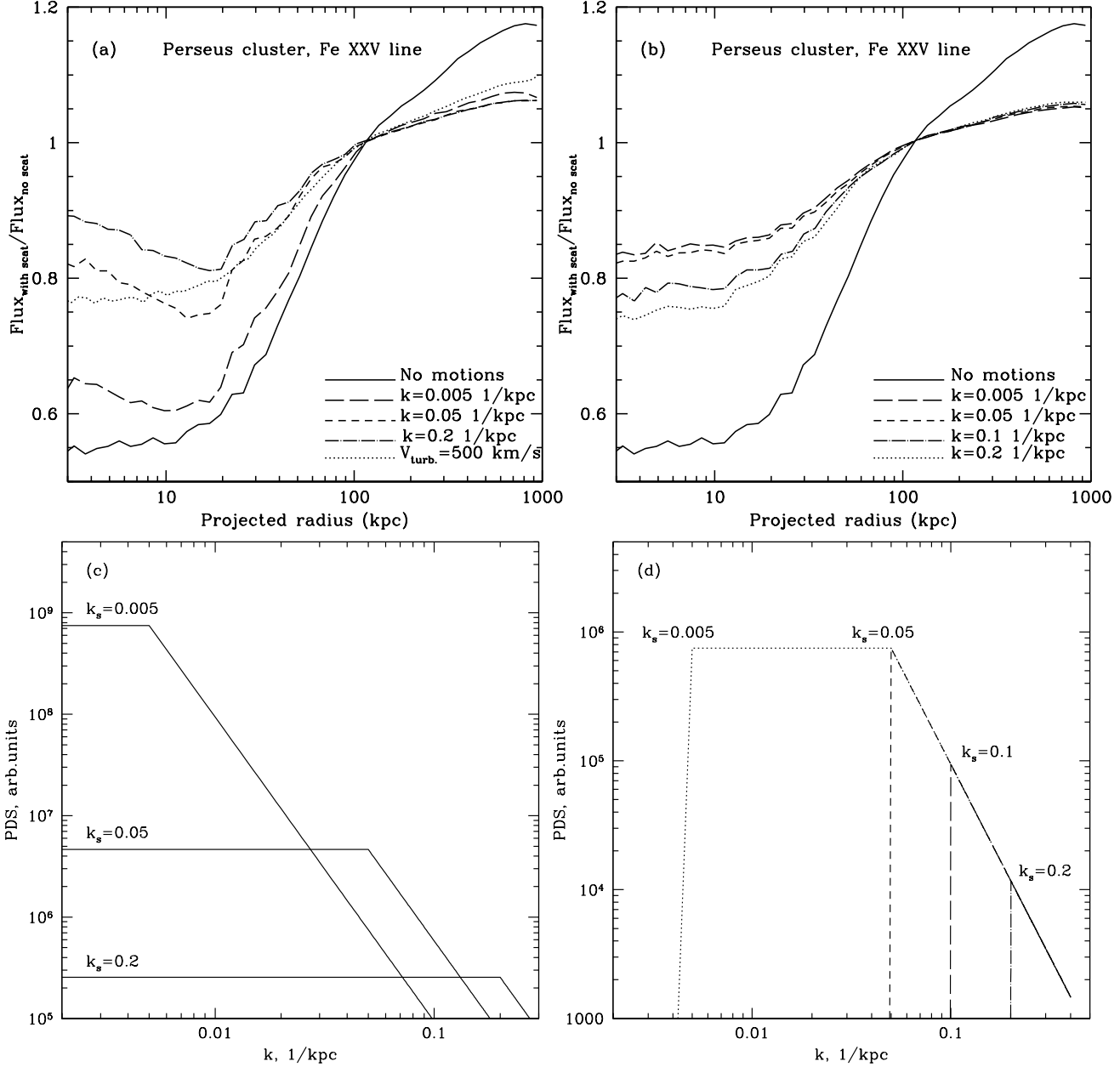


Figure 7. The upper panels: the ratio of the fluxes in the helium-like iron FeXXV line at 6.7 keV with and without scattering in the cluster A426 for gas motions on various scales. The left upper panel: the sensitivity to large-scale motions (case B, see the “Results” Section). The curves correspond to different values of k_s (see the lower left panel). The curve for microturbulence is presented for comparison. The right upper panel: the sensitivity to small-scale motions when the power spectrum (see the lower right panel) of the velocities of gas motions is cut off at various k (case C, see the “Results” Section). The lower panels: the power spectra of the velocities of gas motions in galaxy clusters assumed in the calculations. The left lower panel: the power spectrum is flat at small k_s ($=0.005, 0.05$, and 0.2) and then falls off as the Kolmogorov one (see the “Results” Section). The right lower panel: the power spectrum for $k_s = 0.05$ (see the left panel) is cut off at $k > 0.005, 0.05, 0.1$ and 0.2 (see the “Results” Section).

of the motions are larger than r_c) inside which the scattering actually takes place. An increase in k_s , i.e. assuming the power spectrum to be flat at small k (with the total energy of the motions conserved), leads to suppression of the role of large-scale motions and to an increase in the velocity dispersion on small scales. This immediately leads to a decrease in the optical depth in the line and resonance

scattering effect is less strong (the curve with short dashes and the dash-dotted curve; the dotted curve is drawn for comparison with the case of isotropic microturbulence).

We also see from Fig. 8b that the earlier we “cut off” the power spectrum (case C), i.e. the larger the power is in the small-scale motions affecting the line broadening, the weaker is the resonant scattering.

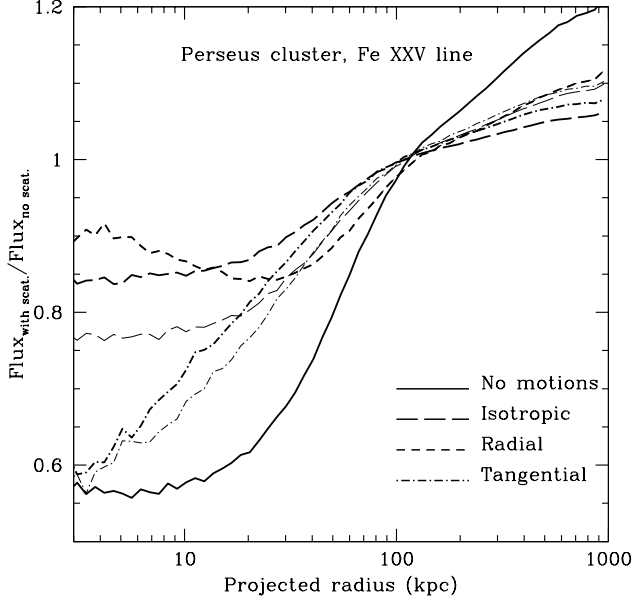


Figure 8. Ratio of the fluxes in the helium-like iron FeXXV line at 6.7 keV with and without scattering in the cluster A426 for isotropic, radial, and tangential microturbulent gas motions (case A). The thick and thin curves correspond to the cases of fixed velocity amplitude and fixed total kinetic energy, respectively.

6 CONCLUSIONS

We considered the influence of large- and small-scale anisotropic gas motions on the resonant scattering in the FeXXV line at 6.7 keV for the Perseus cluster as an example. The model velocity field is taken from the results of hydrodynamic simulations of galaxy cluster formation (Dolag et al. (2005)).

We showed that (1) the resonant scattering is sensitive mainly to small-scale gas motions, (2) it is particularly sensitive to radial motions, (3) large-scale gas motions affect mainly the shift of the line center and (4) the directions of small-scale motions can be estimated by considering the broadening of spectral lines and the resonant scattering in lines simultaneously.

The sensitivity to anisotropy of microturbulent motions is illustrated by the following example: at fixed total kinetic energy corresponding to $V_{\text{rms}} = 500 \text{ km s}^{-1}$, the expected decrease in FeXXV line flux at the center ($R < 10 \text{ kpc}$) of the cluster A426 is a factor of 0.77, 0.9 and 0.61 for isotropic, radial, and tangential turbulence, respectively. At fixed velocity dispersion in one direction (Eq. (7)), the corresponding decreases are a factor of 0.84, 0.9, and 0.63, respectively. In other words, if a significant anisotropy of small-scale gas motions is allowed, then the same ratio of the line fluxes corresponds to different characteristic velocity amplitudes. For example, for the case considered above (Fig. 7), approximately the same ratio of the line fluxes from a region 10 kpc in radius arises at $V_{\text{rms}} = 500 \text{ km s}^{-1}$ for isotropic motions, $V_{\text{rms}} \approx 200 \text{ km s}^{-1}$ for radial motions, and $V_{\text{rms}} \approx 1700 \text{ km s}^{-1}$ for tangential motions. Note that such a large dif-

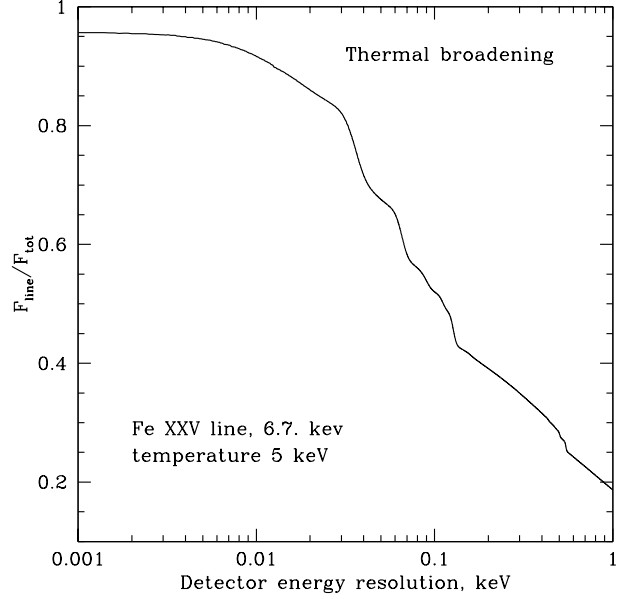


Figure 9. Ratio of the FeXXV line flux to the total flux, including the continuum and neighboring lines, versus detector energy resolution for a cluster with a mean temperature of 5 keV. Only the thermal line broadening is taken into account.

ference is related, in particular, to a nonlinear dependence of the line flux ratio on the velocity of gas motions. For a larger region ($r < 30 \text{ kpc}$), a comparable line flux ratio arises at $V_{\text{rms}} = 500 \text{ km s}^{-1}$ (isotropic motions), $V_{\text{rms}} \approx 300 \text{ km s}^{-1}$ (radial motions), and $V_{\text{rms}} \approx 1200 \text{ km s}^{-1}$ (tangential motions). In this case, the difference between the velocity amplitudes is about a factor of 4. Of course, the presence of purely radial or purely tangential motions in clusters is unlikely and the typical uncertainty is not so great. Note also that the results of our calculations, obtained under the assumption of isotropic gas motions, can be used to set conservative upper limits on the amplitude of purely radial motions, while robust constraints on the amplitude of tangential motions are difficult to obtain from resonant scattering observations.

Large-scale gas motions affect weakly the scattering efficiency. For example, we see from Fig. 8a that if the whole power of the motions is on scales of 200 kpc, then the scattering efficiency at the cluster center is a factor of 1.13 lower than that in the case when the gas is at rest. In contrast, if the bulk of the power is concentrated on small scales, for example, on scales of $\sim 5 \text{ kpc}$, then the scattering efficiency decreases by a factor of 1.56 (see Figs. 8a and 8b).

Note that the considered line of helium-like iron at 6.7 keV has bright forbidden and intercombination lines as well as satellites. The optical depths of the forbidden and intercombination ($1s^2 - 1s2p(^3P_0)$) lines are almost zero, while the oscillator strength of the intercombination ($1s^2 - 1s2p(^3P_1)$) line is a factor of 10 smaller than that of the resonance line and its optical depth is ~ 0.26 . The satellites correspond to the transitions from excited states

and have a negligible optical depth at a low matter density. Thus, only the resonance transition is essentially involved in the scattering itself. Clearly, the lower the detector energy resolution, the more difficult to measure the suppression of the flux in the resonance line through scattering. In Fig. 9, the ratio of the 6.7 keV line flux to the total flux, including the continuum and neighboring lines, $F_{\text{line}}/F_{\text{tot}}$ is plotted against the detector energy resolution. We see that the 6.7 keV line flux for a cluster with a mean temperature of ~ 5 keV accounts for 50% of the total incoming flux in the energy range $E_0 \pm \Delta/2$ even at an energy resolution $\Delta \sim 100$ eV.

Apart from their influence on the surface brightness profile, gas motions change the degree of polarization in X-ray lines, which results from resonant scattering in the presence of a quadrupole moment in the radiation field. Zhuravleva et al. (2010) showed that in the presence of isotropic microturbulent or large-scale gas motions, the degree of polarization in galaxy clusters can decrease by several times. Clearly, depending on the directions of microturbulent motions, the degree of polarization will also change.

7 ACKNOWLEDGEMENTS

This study was supported by the RAS Programs P19 and DPS 16, the Program for Support of Leading Scientific Schools (grant NSH-5069.2010.2), and the Russian Foundation for Basic Research (project no. 09-02-00867-a). S. Sazonov is grateful to the Dynasty Foundation for support. I. Zhuravleva is grateful to the International Max Planck Research School (IMPRS).

REFERENCES

- E. Anders and N. Grevesse, *Geochim. Cosmochim. Acta* 53, 197 (1989).
- P. Arevalo et al., *Astrophys. J.* (2011, submitted).
- M. Asplund, N. Grevesse, A. J. Sauval and P. Scott, *Ann. Rev. Astron. Astrophys.* 47, 481 (2009).
- S. Chandrasekhar, *Radiative Transfer* (Clarendon, Oxford, 1950).
- E. Churazov, M. Brueggen, C. R. Kaiser et al., *Astrophys. J.* 554, 261 (2001).
- E. Churazov, W. Forman, C. Jones and H. Boehringer, *Astrophys. J.* 590, 225 (2003).
- E. Churazov, W. Forman, C. Jones et al., *Mon. Not. R. Astron. Soc.* 346, 29 (2004).
- E. Churazov, R. Sunyaev, W. Forman and H. Boehringer, *Mon. Not. R. Astron. Soc.* 332, 792 (2002).
- E. Churazov, I. Zhuravleva, S. Sazonov and R. Sunyaev, *Space Sci. Rev.* 104 (2010).
- K. Dolag, F. Vazza, G. Brunetti and G. Tormen, *Mon. Not. R. Astron. Soc.* 364, 753 (2005).
- A. C. Fabian, J. S. Sanders, S. W. Allen et al., *Mon. Not. R. Astron. Soc.* 344, L43 (2003).
- A. C. Fabian, J. S. Sanders, G. B. Taylor et al., *Mon. Not. R. Astron. Soc.* 366, 417 (2006).
- W. Forman, C. Jones, E. Churazov et al., *Astrophys. J.* 665, 1057 (2007).
- W. Forman, P. Nulsen, S. Heinz et al., *Astrophys. J.* 635, 894 (2005).
- M. R. Gilfanov, R. A. Sunyaev and E. M. Churazov, *Sov. Astron. Lett.* 13, 3 (1987).
- D. R. Hamilton, *Astrophys. J.* 106, 457 (1947).
- N. A. Hatch, C. S. Crawford, A. C. Fabian, R. M. Johnstone, J. S. Sanders, proceedings of the The X-ray Universe 2005 (ESA SP-604), ed. A. Wilson, 604, 689 (2006).
- N. A. Inogamov and R. A. Sunyaev, *Astron. Lett.* 29, 791 (2003).
- M. Markevitch and A. Vikhlinin, *Phys. Rev.* 443, 1 (2007).
- P. Mazzotta, G. Mazzitelli, S. Colafrancesco and N. Vittorio, *Astron. Astrophys.* 133, 403 (1998).
- K. Mitsuda, High Resolution X-ray Spectroscopy: Towards IXO, proceedings of the international workshop held at the Mullard Space Science Laboratory of University College London, ed. G. Branduardi-Raymont and A. Blustin (2009).
- M. L. Norman and G. L. Bryan, *Numerical Astrophysics : Proceedings of the International Conference on Numerical Astrophysics held at the National Olympic Memorial Youth Center*, ed. Shoken M. Miyama, Kohji Tomisaka and Tomoyuki Hanawa, *Astrophysics and space science library*, v. 240, p.19 (1999).
- L. A. Pozdnyakov, I. M. Sobol and R. A. Sunyaev, *Astrophys. Sp. Phys. Rev.* 2, 189 (1983).
- P. Rebusco, E. Churazov, R. Sunyaev et al., *Mon. Not. R. Astron. Soc.* 384, 1511 (2008).
- J. S. Sanders, A. C. Fabian, R. K. Smith and J. R. Peterson, *Mon. Not. R. Astron. Soc.* 402, L11 (2010).
- S. Y. Sazonov, E. M. Churazov and R. S. Sunyaev, *Mon. Not. R. Astron. Soc.* 333, 191 (2002).
- P. Schuecker, A. Finoguenov, F. Miniati et al., *Astron. Astrophys.* 426, 387 (2004).
- R. K. Smith, N. S. Brickhouse, D. A. Liedahl and J. C. Raymond, *Astrophys. J.* 556, L91 (2001).
- V. Springel, N. Yoshida and S. D. M. White, *New Astron.* 6, 79 (2001).
- F. Vazza, G. Brunetti, A. Kritsuk et al., *Astron. Astrophys.* 504, 33 (2009).
- S. Vogt and T. A. Enßlin, *Astron. Astrophys.* 412, 373 (2003).
- N. Werner, I. Zhuravleva, E. Churazov et al., *Mon. Not. R. Astron. Soc.* 398, 23 (2009).
- H. Xu, S. M. Kahn, J. R. Peterson et al., *Astrophys. J.* 579, 600 (2002).
- I. Zhuravleva, E. Churazov, S. Sazonov et al., *Mon. Not. R. Astron. Soc.* 403, 129 (2010).
- I. Zhuravleva et al., (2011, in preparation).